Reinforcement effect of STF on impact properties of aramid, basalt, and carbon fiber reinforced polymer using SHPB

zhiping huang
Jishou University
Minghai Wei (wei.mgh@zstu.edu.cn)
Zhejiang Sci-Tech University
Junyu Chen
Jishou University
Wanjin Gu
Zhejiang Sci-Tech University
Fang Zhu
Jishou University

Research Article

Keywords: Shear thickening fluid, FRP, High strain rate, Energy absorption efficiency, Strain rate effect

Posted Date: May 2nd, 2023

DOI: https://doi.org/10.21203/rs.3.rs-2855326/v1

Abstract

The objective of this research is to characterize the high strain rate impact performance of fiber-reinforced polymer (FRP) impregnated with shear thickening fluid (STF) by using a split Hopkinson pressure bar (SHPB) test. Three types of FRP with aramid, basalt, and carbon fibers are prepared, followed by impregnated with 15 wt.% STF and 20 wt.% STF to develop FRP composited materials (FRP-STF), respectively. The results demonstrate that STF impregnated significantly enhances the high strain rate impact performance for the AFRP, BFRP, and CFRP. Nevertheless, the enhancing effect is different for different types of FRP. Under 3800 s^{-1}, when the mass fraction of STF is 20%, the increase rate of BFRP stress peak is the highest, reaching 58.9%. However, the best increase of energy absorption peak is AFRP, reaching 226.8%. Under 6100 s^{-1}, the stress response of AFRP-20%STF is the best, and the energy absorption peak of CFRP-20%STF reaches 710.5 J, about 2.3 times that of pure CFRP. This is also reflected in the energy absorption per unit density curve. The results also show three FRPs have significant strain rate effects, especially on the energy absorption peak. The maximum increase rates are 101.9%, 710.7%, and 1070.5%, respectively.

1. Introduction

Fiber-reinforced polymer (FRP) composites, including aramid (AFRP), basalt (BFRP), carbon (CFRP), and glass (GFRP) fibers, have been widely used in structural members bearing quasi-static loads due to their superior specific strength and stiffness [1–4]. However, in many cases, FRP used in aerospace, pipeline, and military applications is vulnerable to high strain rate loads such as high-velocity impact or explosion. At this time, compared with other ductile materials, such as metals, FRP usually has poor impact mechanical properties and is easy to fracture [5, 6]. The main reason for this brittle fracture is that the initial internal defects in the fiber do not have enough time to release under the high strain-rate impact, leading to the premature failure of its composite [7, 8], which limits the application of FRP in the high strain rate loading environment.

In recent years, a new smart material, shear thickening fluid (STF), has been widely used in energy absorption research [9–14]. STF is usually a highly concentrated colloidal suspension composed of microparticles and nanoparticles uniformly dispersed in a specific dispersion medium [15–17]. Under external shear, the apparent viscosity of STF generally rises hundreds of times, and the response is fast and sensitive. It is important to have self-recovery characteristics after the external load disappears [18]. Compared with liquid, STF has the advantage of withstanding greater external force, and compared with solid, it has the characteristics of an unfixed shape. Therefore, STF has a broad application prospect in high-velocity impact resistance [19–21].

Regarding the STF strain rate effect, Lima et al. [22] found that the strain rate influenced both continuous and discontinuous silica-based STF (SiO_2-STF). The compressive stress-strain curve of the former became extreme or even discontinuous with the increase of its particle volume fraction. At the same time, the transition time for shear thickening in the latter decreased logarithmically with the loading

compression rate. The authors emphasized that these results are significant for engineering applications of STF involving high-velocity and immediate impacts at last. Conversely, Jiang et al. [23] studied the mechanical properties of SiO_2-STF extruded at high strain rates using a split Hopkinson pressure bar (SHPB) apparatus. They reported a liquid-to-solid transition in the properties of STF, which increased the impact strength. At the same time, their work also showed that although the bulk modulus of STF increased with the increase in strain rate, the volume fraction had little effect on the bulk modulus. Similarly, the team of Asija et al. [24] used SHPB to study stress-strain behavior and impact toughness changes at high strain rates of SiO_2-STF. The results indicated that the impact toughness of STF increased with the increase in loading rate, and the peak stress corresponding to the maximum strain rate was 147 MPa. Their work [25] likewise confirmed that the stress and impact toughness of STF under high strain rates were directly related to the SiO_2 particle size. In contrast, the time for liquid-to-solid state transition decreased along with the reduction of SiO_2 particle size.

In terms of high-velocity impact resistance, Lee et al. [26] made a pioneering study on STF-impregnated Kevlar fabric (Kevlar-STF) and found that SiO_2 nanoparticles in STF could effectively prevent the relative slip of yarn caused by high-velocity impact after Kevlar-STF was impacted. As a result, more fibers in the yarn absorb energy through tensile deformation. Therefore, STF can effectively improve Kevlar's ballistic performance. At the same time, Kevlar-STF fabric is superior to pure Kevlar fabric under the same conditions in terms of thickness and softness. Park et al. [27, 28] performed high-velocity impact tests on Kevlar-STF fabric under the impact velocity of 1000 ~ 2000 m/s. This confirmed that STF could significantly increase the energy absorption capacity of Kevlar fabric, and its energy absorption capacity can reach up to about 70%. Haris et al. [29] studied the effect of various STFs on the ballistic penetration performance of STF-Kevlar® composites. They showed that only when the particle volume fraction reaches a certain high-volume fraction can the excellent ballistic penetration performance of the composites be reflected. Hasan Nezhad et al. [20] studied the ballistic and cushioning properties of GFRP impregnated with pure shear thickening fluid and treated shear thickening fluid, respectively through an air gun and drop hammer impact tests. Ballistics tests show that STF can effectively reduce the penetration depth of GFRP, and the performance of STF has a significant impact on the ballistic performance.

It can be seen from the above literature that STF has a significant strain rate effect and can effectively improve the ballistic impact mechanical properties of Kevlar fabrics. However, STF is rarely used in the FRP field, especially in high strain rate loading. Therefore, the primary purpose of this work is to study the mechanical behavior of AFRP-STF, BFRP-STF, and CFRP-STF composites under high strain rate impact. Using pure AFRP, BFRP, and CFRP specimens as reference materials, the mechanical properties of FRP-STF under different high strain rate were tested by SHPB. The effects of high strain rate and STF mass fraction on the impact mechanical properties of the three FRP-STFs were discussed from the stress response, strain energy absorption, energy absorption rate, and strain rate effect.

2. Experimental methods

2.1 Materials

In this work, the raw materials for preparing STF are SiO_2 nanoparticles and polyethylene glycol (PEG200). The original particle size of SiO_2 nanoparticles is 12 nm, the relative density is 2.319 ~ 2.653, and the pH value is 3.7 ~ 4.7. It is a hydrophilic fumed silica. The hydroxyl value of PEG200 is 510 ~ 623 mg KOH/g, and it is a stable, transparent liquid at room temperature.

Table 1
Detail of FRPs parameters

Types	Aerial densities (g/m^2)	Monolayer thicknesses (mm)	Elastic module (GPa)	Failure elongations (%)
AFRP	280	0.193	110	2.0
BFRP	300	0.170	91	2.6
CFRP	300	0.167	210	1.5

Three types of FRP, including AFRP, BFRP, and CFRP, are woven, plain woven, and unidirectional, respectively. The detail of the FRPs parameters is given in Table 1. Also, absolute ethanol AR (analytical reagent) is used to dilute STF when preparing FRP-STF composites.

2.2 STF preparation and rheological characteristic

The preparation of STF requires that the dispersed phase particles be uniformly dispersed in the dispersion medium to keep their rheological properties stable. The specific process is as follows: first, put SiO_2 nanoparticles into a vacuum drying oven and dry it at 110 ℃ for 12 hours to remove their moisture; Secondly, according to the required STF mass fraction, weigh a certain amount of SiO_2 and PEG200 and pour them into the beaker in batches, continue to stir until uniform mixing, and then add the next batch; Finally, put the obtained STF into a vacuum drying oven to remove its bubbles, and a stable STF can be obtained.

The rheological behavior of the STFs is given in Fig. 1. It can be seen that the viscosity curves of 15wt.% STF (15%STF) and 20wt.% STF (20%STF) shows the following changes with the shear rate: when the shear rate is low, the viscosity decreases with the increase of the shear rate, showing a significant shear thinning behavior; When the shear rate increases to a critical value, the viscosity increases by leaps and bounds, showing a significant thickening phenomenon; After the shear rate is further increased to the shear rate corresponding to the peak viscosity, the viscosity of STF has been dramatically reduced due to the destruction of its internal "particle cluster" mechanism by external forces. The above phenomena indicate that both 15wt.% STF and 20wt.% STF prepared in this work have a significant shear thickening effect. Importantly, the viscosity peak 20wt.% STF is 79.9 Pa s, an increase of 53.9% compared to 15wt.% STF, the corresponding critical shear rate is ahead by about 20.5%.

2.3 FRP impregnation and microscopy characteristics

The FRP used in the impact test is a type of unidirectional AFRP, BFRP and CFRP. To fabricate the FRP-STF, which is impregnated by STF, first, cut the FRP into a shape with a diameter of 40 mm and place it in an 80 ℃ vacuum drying oven for 12 hours; Further, in the ultrasonic cleaning machine, FRP is immersed in the STF mixture diluted with absolute ethanol at the mass fraction of 1:1 for 10 minutes to form FRP-STF initially; Then put the FRP-STF in a blast dryer for drying at 85 ℃, and weigh its mass every two hours until the mass does not change; Finally, paste the pure FRP and FRP-STF with thermoplastic polyurethanes hot melt adhesive respectively, and compact all specimens with a flat vulcanizer. Figure 2 shows the significant steps in fabricating the FRP-STF composite materials.

Figure 3 shows the SEM images of neat FRP and FRP-STF composites. In comparison with Figs. 3(a) and (d), Figs. 3(b) and (e), Figs. 3(c) and (f), respectively, the size of the nanoparticles which adhere to filaments is much smaller than the diameter of the filaments. Moreover, a large number of the silica nanoparticles are distributed on the surface of the filaments and filled in the gap between filaments in the FRP-STF composites (Seen in Figs. 3(d)-(f)), indicating that the STF-impregnated FRP are composited successfully by the STF and will have excellent mechanical performance since these particles enhance the bonding between fibers. Figure 3 also showed that the fiber spacing in BFRP is large, and the fiber spacing in CFRP is the tightest, followed by AFRP, indicating that the three fibers' overall stress will be significantly different.

2.4 SHPB impact testing

The SHPB apparatus used in this test is shown in Fig. 4. The whole test system consists of a loading device, a pressure bar device, and a data acquisition system. The pressure bar device comprises an incident bar, a transmission bar, an absorption bar, and an end-damping device. In the test, all rods are aluminum with a diameter of 40 mm, an elastic modulus of 70 GPa, a density of 2.71 g/cm^3, and a wave velocity of 5218 m/s. The length of the incident rod and transmission shaft is 1800 mm. In addition, considering using a shaper to control the loading wave, the length of the impact rod is 300 mm. The loading device uses high-pressure purified nitrogen as the power source and calculates the strain rate corresponding to the air pressure through the data acquisition system. The strain rate is 3800 s^{-1}, 4100 s^{-1}, 5100 s^{-1}, and 6100 s^{-1}.

3. Results and discussion

3.1 Impact response under high strain rate

The stress vs. strain responses and energy absorbed performance of the AFRP-STF, BFRP-STF, and CFRP-STF specimens with a different mass fraction of STF under 3800 s^{-1} are presented respectively in Figs. 5 and 6 and Table 2.

Table 2 Impact response of AFRP-STF, BFRP-STF, and CFRP-STF at a strain rate of 3800 s^{-1}.

	AFRP			BFRP			CFRP		
STF	0%	15%	20%	0%	15%	20%	0%	15%	20%
Peak stress (MPa)	120.8	123.2	161.7	78.3	105.1	124.4	168.1	100.2	119.3
Peak absorbed energy (J)	51.9	79.0	169.6	22.8	81.5	61.4	107.2	23.7	60.7
Absorbed energy per unit density (J cm^3/g)	11.9	18.2	39.0	4.3	15.4	11.6	19.9	4.4	11.3

As seen in Fig. 5, the composite of STF has a particular influence on the stress response of AFRP, BFRP, and CFRP under a high strain rate. For AFRP, there is almost no change in the stress behavior after the STF composite, but 20%STF can increase the stress peak of pure AFRP from 120.8 MPa to 161.7 MPa, with an increase of 33.9%. After the BFRP is composited with STF, its stress response changes significantly, especially the 20%STF increases the stress peak by 58.9% compared with the pure BFRP. Although 15%STF only increased the stress peak of BFRP by 4.1%, the stress behavior of BFRP-15%STF showed good ductility characteristics, and its stress did not drop to zero until the strain was 0.258. However, unlike AFRP-STF and BFRP-STF, the addition of STF significantly reduced the stress peak of CFRP by 40.4% (15%STF) and 29.0% (20%STF), respectively, at 3800 s^{-1} impact. As seen in Fig. 9(c), the impact energy of 3800 s^{-1} is insufficient to stimulate a higher stress response of CFRP-STF. In other words, because CFRP fibers are in close contact under the impact, the dispersed phase particles adhered to them are more likely to absorb more impact energy through mutual friction and the "particle cluster" mechanism between particles, so that CFRP itself bears less impact energy and shows a smaller stress peak.

Further seen in Fig. 6, the strain energy absorption capacity of AFRP and BFRP is significantly increased due to the composite of STF. Especially for BFRP, the energy absorption capacity is increased by 257.5% and 169.3% compared with pure BFRP when STF is 15% and 20%, respectively. When the mass fraction of STF is 20%, the energy absorption capacity of AFRP increased by more than 226.8%, and the energy absorption mode was changed. From Fig. 6(a), the energy absorption vs. time curve of AFRP-STF no longer shows a significant decline segment, which is mainly because the SiO_2 nanoparticles adhered to the fiber gather together through fiber deformation, which blocks the transmission of stress waves so that the energy absorption capacity of AFRP-STF continues to increase. In contrast, pure AFRP shows a decline in energy absorption capacity over time because the stress waves directly pass through its fibers. This phenomenon is also reflected in the energy absorption vs. time curves of BFRP-STF and CFRP-STF. As the stress response of CFRP-STF is smaller than that of pure CFRP, it can also be observed that the energy absorption capacity of CFRP-STF is weaker than that of pure CFRP on its energy absorption vs.

time curve. However, the increase of STF mass fraction increases the energy absorption peak of CFRP-STF from 23.7 J to 60.7 J, an increase of nearly 1.6 times.

Figs 7 and 8 and Table 3 show the mechanical impact response of AFRP-STF, BFRP-STF, and CFRP-STF at high strain rates. From Fig. 7, under 6100 s^{-1}, the stress-strain curves of the three kinds of FRP show the same "uplift" phenomenon. Namely, the composite of STF significantly improves the stress response of pure AFRP, BFRP, and CFRP. For example, when the mass fraction of STF is 15%, the stress peaks of the three kinds of FRP are increased by 29.0%, 42.7%, and 22.4%, respectively. However, when the STF mass fraction increases from 15% to 20%, the effects of STF on the three FRP stress peaks are only 7.1%, -20.0%, and 1.7%, which is not as significant as when the strain rate is 3800 s^{-1}. This phenomenon shows that 15%STF and 20%STF have entirely played their strengthening role under high strain-rate impact.

Table 3 Impact response of AFRP-STF, BFRP-STF, and CFRP-STF at a strain rate of 6100 s^{-1}.

	AFRP			BFRP			CFRP		
STF	0%	15%	20%	0%	15%	20%	0%	15%	20%
Peak stress (MPa)	231.7	298.9	315.4	220.0	314.0	270.0	245.1	299.9	306.7
Peak absorbed energy (J)	255.1	449.4	342.4	321.8	537.7	497.8	217.9	684.1	710.5
Absorbed energy per unit density (J cm^3/g)	58.6	103.3	78.7	60.8	101.6	94.0	40.4	126.9	131.8

From Fig. 8, the energy absorption peak of AFRP-STF, BFRP-STF, and CFRP-STF is much greater than that under the impact of 3800 s^{-1}. According to Fig. 9, the above three FRP have been destroyed under the impact of this strain rate. On the other hand, the energy absorption capacity of AFRP, BFRP, and CFRP has been significantly improved after STF composite, e.g., when the STF mass fraction is 20%, the energy absorption peak of the three FRP has been increased by 34.2%, 54.7%, and 226.1% respectively. This improvement is superior to the improvement of their corresponding stress peak. The reason may be that the FRP becomes softer after STF impregnation, and its fracture strain has been dramatically improved. Therefore, the capacity to absorb energy has been significantly improved. In addition, comparing the three FRP, it can be found that the energy absorption of CFRP-STF under 6100 s^{-1} is most significantly improved, reaching 214.0% and 226.1%, respectively, after 15% STF and 20% STF composited. This improvement ability is 2.8 times and 3.2 times that of AFRP-15%STF and BFRP-15%STF, respectively, and further increases to 6.6 times and 4.1 times as STF mass fraction increases to 20%.

Fig. 9 shows the field photos of AFRP-20%STF, BFRP-20%STF, and CFRP-20%STF after the high strain-rate impact test. It can be seen that AFRP-20%STF has a large area of loose behavior, BFRP-20%STF has

been completely broken, and CFRP-20%STF has only a few fibers left. Therefore, the above phenomena indicate that the three specimens have been wholly damaged under 6100 s^{-1} loading.

The mass effect is also studied by dividing the absorbed strain energy with the density of different FRP. After calculation, the AFRP, BFRP, and CFRP densities are 1.45×103, 1.76×103, and 1.80×103 kg/m3, respectively. The strain energy absorption peak of single-layer AFRP-STF, BFRP-STF, and CFRP-STF on the unit density at 3800 s^{-1} and 6100 s^{-1} are shown in Fig. 10. From Fig. 10(a), pure AFRP and AFRP-STF at 3800 s^{-1} have significant energy absorption capacity, especially the latter has more significant energy absorption capacity. For example, the energy absorption capacity of single-layer AFRP-15%STF is 1.96 times and 6.87 times that of BFRP-15%STF and CFRP-15%STF, respectively, and with the increase of STF mass fraction, this multiple was further increased to 4.8 and 4.9. However, when the strain rate increases to 6100 s^{-1}, the energy absorption capacity of AFRP-STF is not as good as that of BFRP-STF and CFRP-STF. Not only is the energy absorption capacity of BFRP-15%STF slightly different from that of AFRP-15%STF, but the energy absorption capacity of CFRP-15%STF is 1.2 times that of AFRP-15%STF. For CFRP-20%STF, this value is further increased to 1.7.

3.2 Energy absorption efficiency

Since the stress limit is an important factor for energy absorption applications, previous research groups introduced the term “energy absorption efficiency” to properly assess the performance of cellular materials for energy absorption [30-32]. The energy absorption efficiency is the stress-normalized energy absorption capacity that can be calculated from the following equation,

$$\eta(\varepsilon) = \frac{1}{\sigma_m(\varepsilon)} \int_0^{\varepsilon} \sigma(\varepsilon) d\varepsilon \qquad (1)$$

where, σ and ε are the compressive stress and strain, respectively, and σ_m is the maximum stress.

Figs. 11 and 12 show the strain energy absorption efficiency curves of AFRP-STF, BFRP-STF, and CFRP-STF at 3800 s^{-1} and 6100 s^{-1}, respectively. From Fig. 11, STF not only significantly improve the limit-strain of three kinds of FRP, but also significantly improve their energy absorption efficiency. Importantly, with the increase of STF mass fraction, the energy absorption efficiency and limit-strain can be further improved. For example, under the impact of 3800 s^{-1}, the maximum energy absorption efficiency of AFRP-15%STF and AFRP-20%STF is 1.4 and 2.9 times that of pure AFRP respectively, and the corresponding limit-strain is extended by 154.5% and 500% respectively.

Compared Fig. 12 to Fig. 11, under the impact of 6100 s-1, STF has a more significant effect in improving the energy absorption efficiency and extending the limit-strain of FRP, e.g., the energy absorption efficiency and limit-strain of AFRP-15%STF are 4.2 times and 3.0 times of those under 3800 s^{-1}, respectively. Comparing the three kinds of FRP, it can be found that CFRP-20%STF has the best energy

absorption efficiency under the impact of high strain rate, reaching 2.3, and STF has the most significant effect in improving its energy absorption efficiency, 4.3 times that of pure CFRP.

Taking AFRP-20%STF, BFRP-20%STF, and CFRP-20%STF as examples, Fig. 13 shows the effect of strain rate on the impact mechanical properties of the three FRP-STF. It can be seen that both the stress peak value and the energy absorption peak value of FRP-STF have significant strain rate effects. Overall, the strain-rate effect of the three FRP-STFs is relatively consistent, but when the strain rate increases from 3800 s^{-1} to 6100 s^{-1}, the peak stress increases by 95.1%, 117.0%, and 157.1%, respectively. For AFRP-STF and CFRP-STF, the maximum increase rate of stress peak caused by the increase of strain rate is 65.2% and 81.7%, respectively, and both occur when the strain rate increases from 3800 s^{-1} to 4100 s^{-1}. However, it is known from Fig. 13 (b) that the strain energy absorption peak of AFRP-STF is less sensitive than that of BFRP-STF and CFRP-STF to the increase in strain rate. Significantly when the strain rate increases from 5100 s^{-1} to 6100 s^{-1}, the energy absorption peak of BFRP-STF and CFRP-STF increases by 107.5% and 102.6%, respectively, and is 3.4 times and 3.3 times AFRP-STF. Importantly, the energy absorption peak of AFRP-STF only increased by 1.0 times, while that of BFRP-STF and CFRP-STF increased by 7.1 times and 10.7 times, respectively, during the whole process of strain-rate increase.

4. Conclusions

The high strain rate impact performance of three FRP styles, including AFRP, BFRP, and CFRP, are investigated with SHPB tests before and after STF impregnation. The STF was synthesized by dispersing 15.0 wt.% and 20.0 wt.% of 12 nm silica in PEG200, respectively, and rheological tests showed that the viscosity of both STFs exhibited a significant shear thickening effect. The SHPB test results demonstrate that STF significantly enhances the impact response of these FRP, but the enhancing effect is different for different types of FRP.

AFRP-STF, BFRP-STF, and CFRP-STF have significant strain-rate effects on stress response and energy absorption performance, but under the high strain-rate impact, BFRP-20%STF and CFRP-20%STF are more sensitive to strain-rate effects than AFRP-20%STF. Under 3800 s^{-1}, AFRP-20% STF has the best performance in stress response, with peak stress of 161.7 MPa, 1.3 times that of pure AFRP. However, the effect of STF on increasing the stress peak value is BFRP-20%STF, which is 58.9% higher than that of pure BFRP. The mechanical properties of AFRP-STF, BFRP-STF, and CFRP-STF under 6100 s^{-1} are better than those of 3800 s^{-1}, which indicates that FRP-STF is more suitable for a high strain-rate loading environment. Although the stress peaks of the three FRP-STFs under 6100 s^{-1} impact have little difference, the strain energy absorption capacity of CFRP-STF is the most significant, reaching 710.5 J, 3.3 times that of pure CFRP. The strain energy absorption per unit density of single layer AFRP-20%STF is optimal under the impact of 3800 s^{-1}. However, under 6100 s^{-1}, CFRP-STF is superior to that of AFRP-STF and BFRP-STF, 3.5 times and 4.2 times the improved capacity of AFRP-15%STF and BFRP-15%STF, respectively. In addition, STF can significantly improve the limit-strain of AFRP-STF, BFRP-STF, and CFRP-STF under the high strain-rate impact and significantly improve the energy absorption rate of three FRP.

However, the best energy absorption rate under 3800 s^{-1} and 6100 s^{-1} impact is AFRP-20%STF and CFRP-20%STF, respectively.

Declarations

Ethics approval and consent to participate

The authors declare that the submitted manuscript does not involve human or animal research.

Data availability statement

The raw/processed data required to reproduce these findings cannot be shared as the data also forms part of an ongoing study. The relevant data can be made available on request.

Declaration of competing interest

The authors declare that they have no known competing financial interests or personal relationships that could have appeared to influence the work reported in this paper.

Acknowledgments

The authors acknowledge financial support from the Hunan Provincial Department of Education Project [grant number 18C0562] and supported by Natural Science Foundation of Zhejiang Province [grant number LY23E080011].

Funding statement

This work was supported by the Hunan Provincial Department of Education Project [grant number 18C0562] and supported by Natural Science Foundation of Zhejiang Province [grant number LY23E080011].

Authors' contributions

Zhiping Huang contributed significantly to analysis and manuscript preparation.

Minghai Wei contributed to the conception of the study; helped perform the analysis with constructive discussions.

Junyu Chen performed the experiment; performed the data analyses and wrote the manuscript.

Wanjin Gu performed the experiment.

Fang Zhu performed the data analyses

All authors reviewed the manuscript.

References

1. Sun L, Wei M, Zhang N (2017) Experimental study on the behavior of GFRP reinforced concrete columns under eccentric axial load. Constr Build Mater 152:214–225
2. Wei M, Sun L, Zhang C, Wang Q (2017) Effect of seawater exposure on compressive behavior of concrete columns reinforced longitudinally with glass fiber reinforced polymer bars. J Compos Mater:002199831774295
3. Wei Y, Bai J, Zhang Y, Miao K, Zheng K (2021) Compressive performance of high-strength seawater and sea sand concrete-filled circular FRP-steel composite tube columns. Eng Struct 240:112357.
4. Min J, Hu J, Sun C, Wan H, Liao P, Teng H, Lin J (2022) Fabrication processes of metal-fiber reinforced polymer hybrid components: a review. Adv Compos Hybrid Mater 5 (2):651-678.
5. Ahmed A, Zillur Rahman M, Ou Y, Liu S, Mobasher B, Guo S, Zhu D (2021) A review on the tensile behavior of fiber-reinforced polymer composites under varying strain rates and temperatures. Constr Build Mater 294:123565.
6. Skoczylas J, Samborski S, Kłonica M (2021) A multilateral study on the FRP Composite's matrix strength and damage growth resistance. Compos Struct 263:113752
7. Shokrieh MM, Omidi MJ (2009) Tension behavior of unidirectional glass/epoxy composites under different strain rates. Compos Struct 88 (4):595-601
8. Zhang M, Jiang B, Chen C, Drummer D, Zhai Z (2019) The effect of temperature and strain rate on the interfacial behavior of glass fiber reinforced polypropylene composites: a molecular dynamics study. Polymers 11 (11):1766
9. Daelemans L, Cohades A, Meireman T, Beckx J, Spronk S, Kersemans M, De Baere I, Rahier H, Michaud V, Van Paepegem W, De Clerck K (2018) Electrospun nanofibrous interleaves for improved low velocity impact resistance of glass fibre reinforced composite laminates. Mater Des 141:170-184.
10. Wei M, Lin K, Liu H (2019) Experimental investigation on hysteretic behavior of a shear thickening fluid damper. Struct Control Health Monit 26 (9):e2389.
11. Qin J, Guo B, Zhang L, Wang T, Zhang G, Shi X (2020) Soft armor materials constructed with Kevlar fabric and a novel shear thickening fluid. Compos Part B-Eng 183:107686
12. Wei M, Lin K, Sun L (2022) Shear thickening fluids and their applications. Mater Des 216:110570.
13. Gürgen S, Kuşhan MC (2017) The stab resistance of fabrics impregnated with shear thickening fluids including various particle size of additives. Compos Part A-Appl S 94:50-60
14. Swiderska A, Parzuchowski PG, Zurowski R, Wieclaw-Midor A, Wolosz D (2021) Energy dissipating poly(hydroxyurethane) elastomers-Synthesis, characterization and comparison with shear thickening

fluid materials. Polymer 230.
15. Gürgen S (2019) Tuning the rheology of nano-sized silica suspensions with silicon nitride particles. J Nano Res 56:63-70
16. Wagner NJ, Brady JF (2009) Shear thickening in colloidal dispersions. Phys Today 62 (10):27-32
17. Wei M, Lv Y, Sun L, Sun H (2020) Rheological properties of multi-walled carbon nanotubes/silica shear thickening fluid suspensions. Colloid Polym Sci 298:243-250
18. Waitukaitis SR, Jaeger HM (2012) Impact-activated solidification of dense suspensions via dynamic jamming fronts. Nature 487 (7406):205-209
19. Gürgen S (2020) Numerical modeling of fabrics treated with multi-phase shear thickening fluids under high velocity impacts. Thin Walled Struct 148:106573
20. Hasan-nezhad H, Yazdani M, Jeddi M (2022) High- and low-velocity impact experiments on treated STF/3D glass fabrics. Thin Walled Struct 171:108720.
21. Steinke K, Sodano HA (2021) Improved inter-yarn friction and ballistic impact performance of zinc oxide nanowire coated ultra-high molecular weight polyethylene (UHMWPE). Polymer 231.
22. Lim AS, Lopatnikov SL, Wagner NJ, Gillespie JW, Jr. (2010) Investigating the transient response of a shear thickening fluid using the split Hopkinson pressure bar technique. Rheol Acta 49 (8):879-890.
23. Jiang W, Gong X, Xuan S, Jiang W, Ye F, Li X, Liu T (2013) Stress pulse attenuation in shear thickening fluid. Appl Phys Lett 102 (10):101901
24. Asija N, Chouhan H, Gebremeskel SA, Bhatnagar N (2017) High strain rate characterization of shear thickening fluids using Split Hopkinson Pressure Bar technique. Int J Impact Eng 110:365-370.
25. Asija N, Chouhan H, Gebremeskel SA, Bhatnagar N (2017) Influence of particle size on the low and high strain rate behavior of dense colloidal dispersions of nanosilica. J Nanopart Res 19 (1):21.
26. Lee YS, Wetzel ED, Wagner NJ (2003) The ballistic impact characteristics of Kevlar® woven fabrics impregnated with a colloidal shear thickening fluid. J Mater Sci 38 (13):2825-2833
27. Park JL, Yoon BI, Paik JG, Kang TJ (2012) Ballistic performance of p-aramid fabrics impregnated with shear thickening fluid; Part I - Effect of laminating sequence. Text Res J 82 (6):527-541.
28. Park JL, Yoon BI, Paik JG, Kang TJ (2012) Ballistic performance of p-aramid fabrics impregnated with shear thickening fluid; Part II - Effect of fabric count and shot location. Text Res J 82 (6):542-557.
29. Haris A, Lee H, Tay T, Tan V (2015) Shear thickening fluid impregnated ballistic fabric composites for shock wave mitigation. Int J Impact Eng 80:143-151
30. Tan PJ, Harrigan JJ, Reid SR (2002) Inertia effects in uniaxial dynamic compression of a closed cell aluminium alloy foam. Mater Sci Technol 18 (5):480-488.
31. Harris J, Winter R, McShane G (2017) Impact response of additively manufactured metallic hybrid lattice materials. Int J Impact Eng 104:177-191
32. Kader M, Hazell P, Islam M, Ahmed S, Hossain M, Escobedo J, Saadatfar M (2021) Strain-rate dependency and impact dynamics of closed-cell aluminium foams. Materials Science Engineering: A

818:141379

Figures

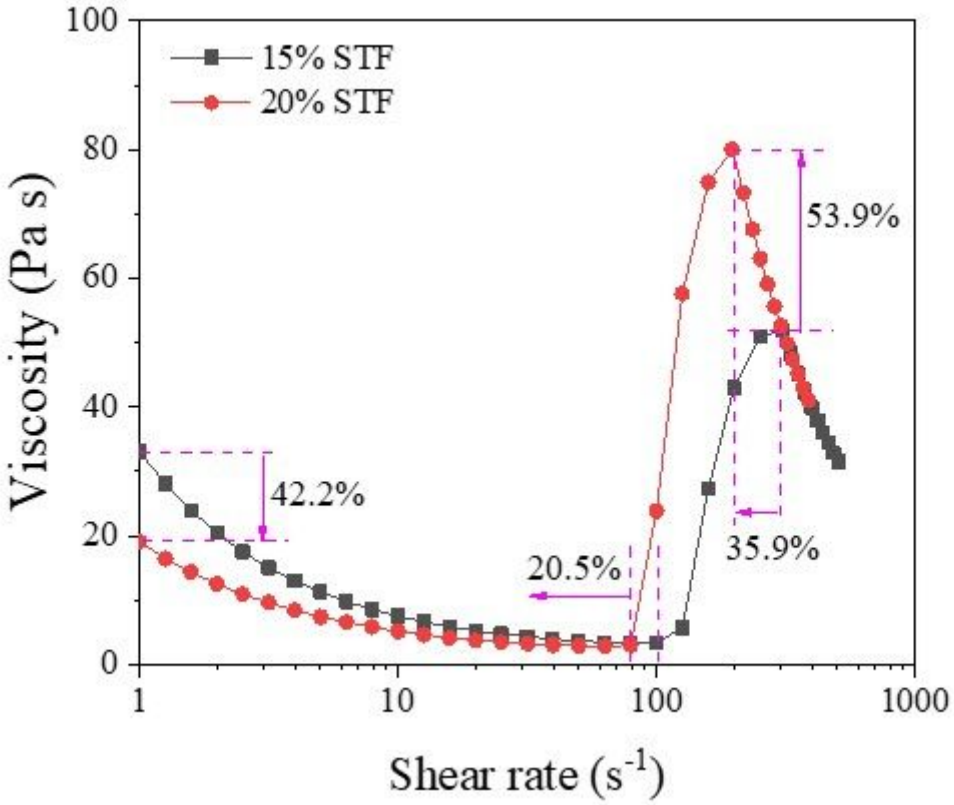

Figure 1

Rheological performance.

Figure 2

Manufacturing procedure of FRP-STF composite samples: (a) 20 wt% STF; (b) AFRP impregnated in diluted STF; (c) AFRP dried in a blast dryer; (d) three layers AFRP-STF specimens. (Take AFRP as an example)

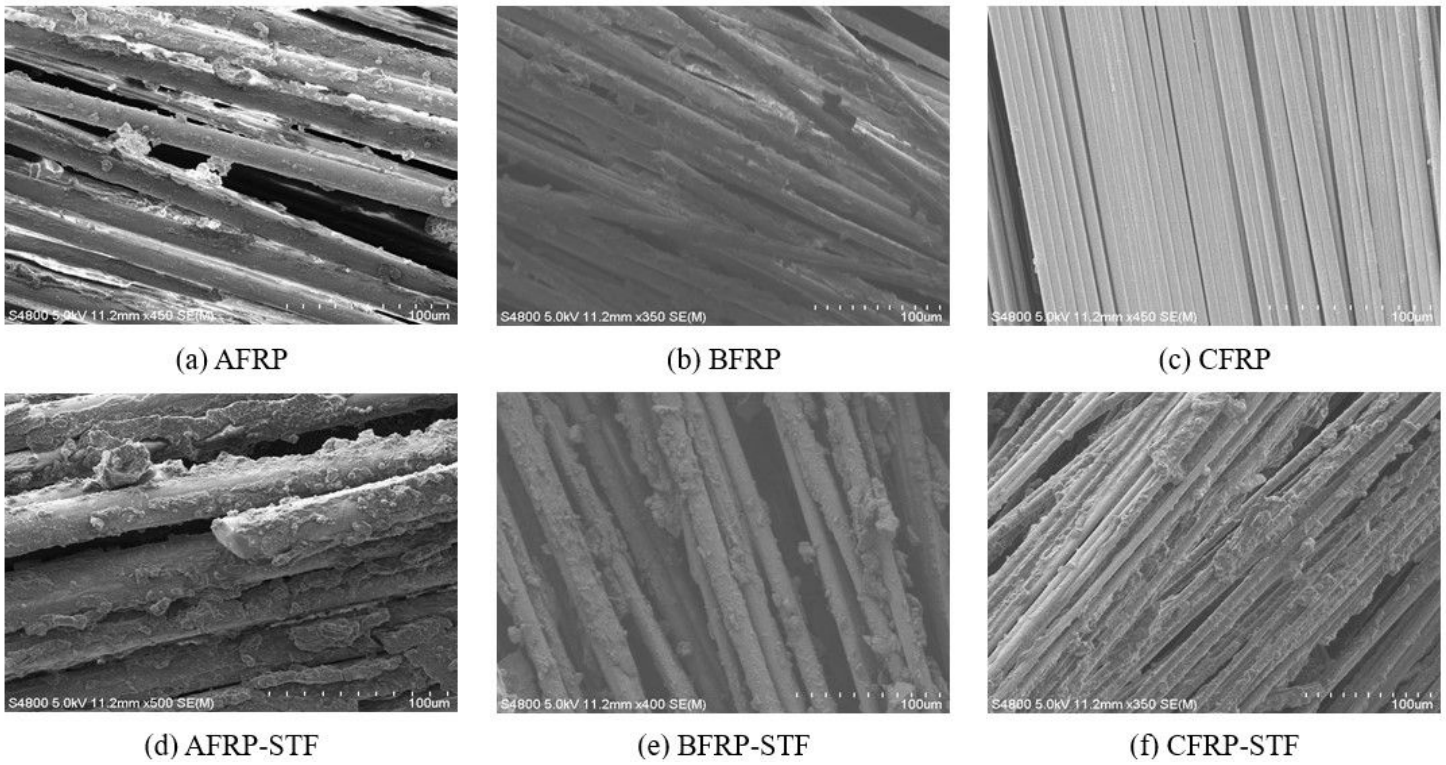

Figure 3

SEM of neat AFRP, BFRP, CFRP, and its corresponding STF composites (100 μm).

Figure 4

High strain impact test setup: (a) SHPB system; (b) strain gauges; (c) test specimen; (d) air pressure device.

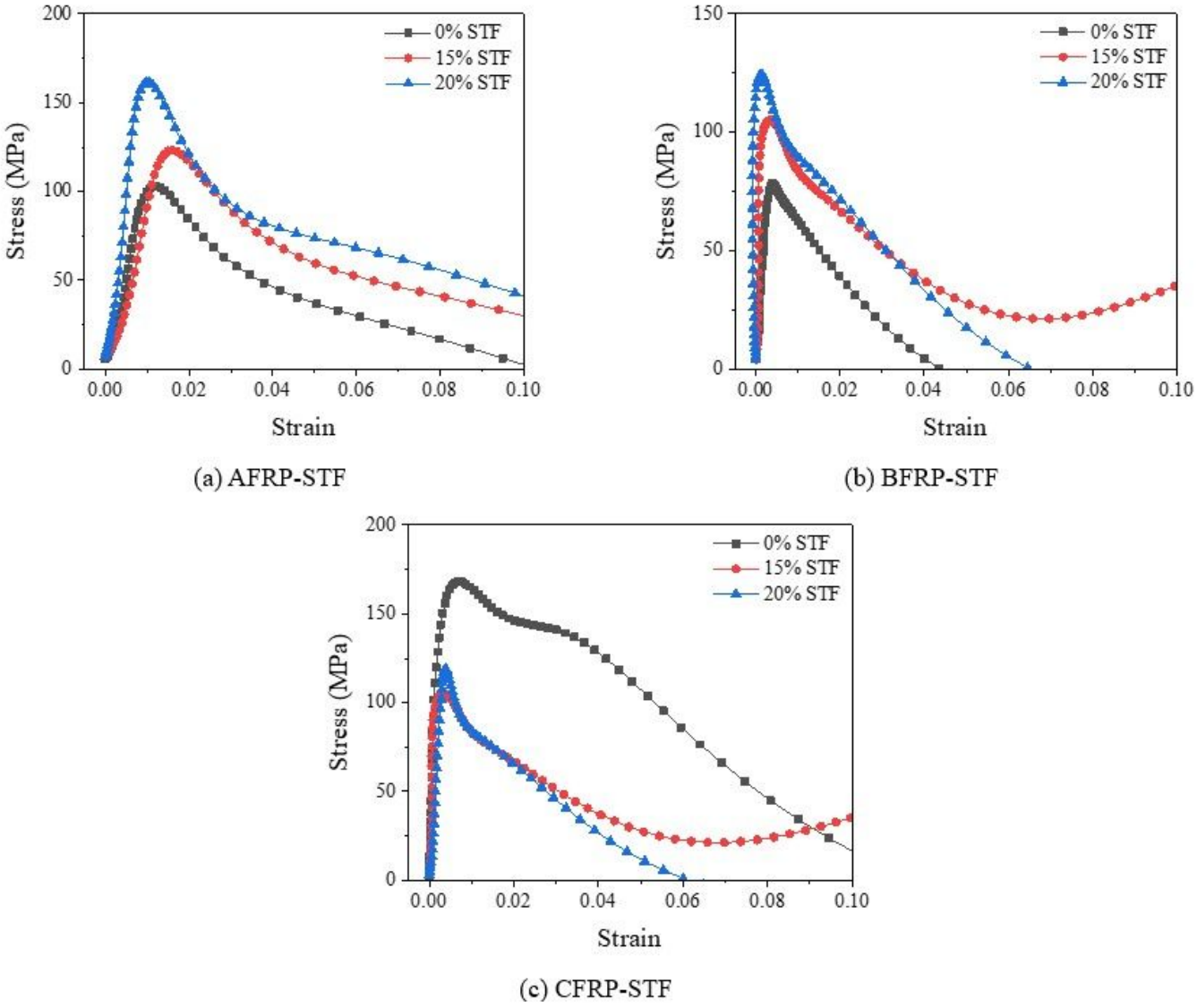

Figure 5

Stress response of AFRP-STF, BFRP-STF, and CFRP-STF at a strain rate of 3800 s^{-1}.

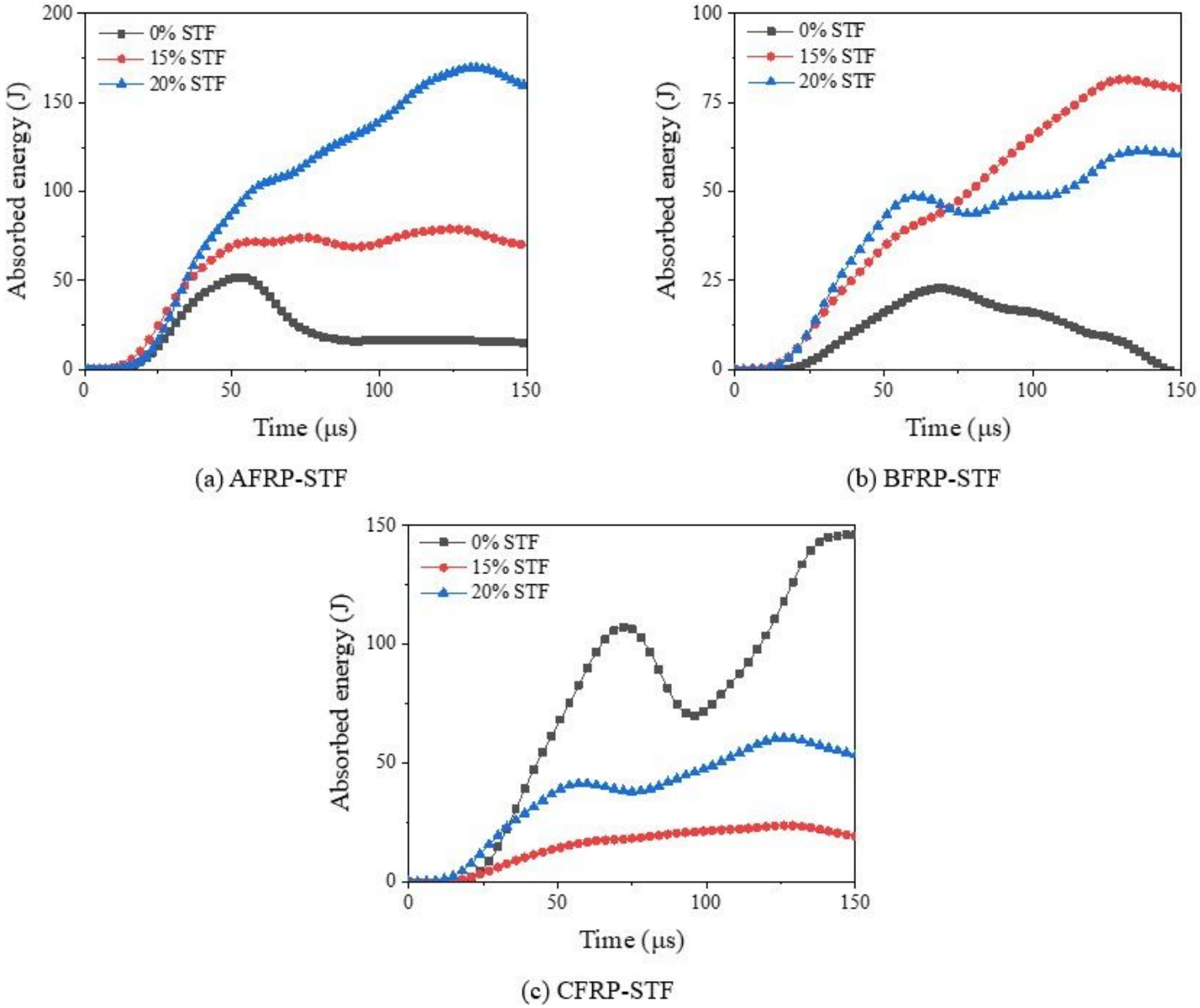

Figure 6

Energy absorption performance of AFRP-STF, BFRP-STF, and CFRP-STF at a strain rate of 3800 s^{-1}.

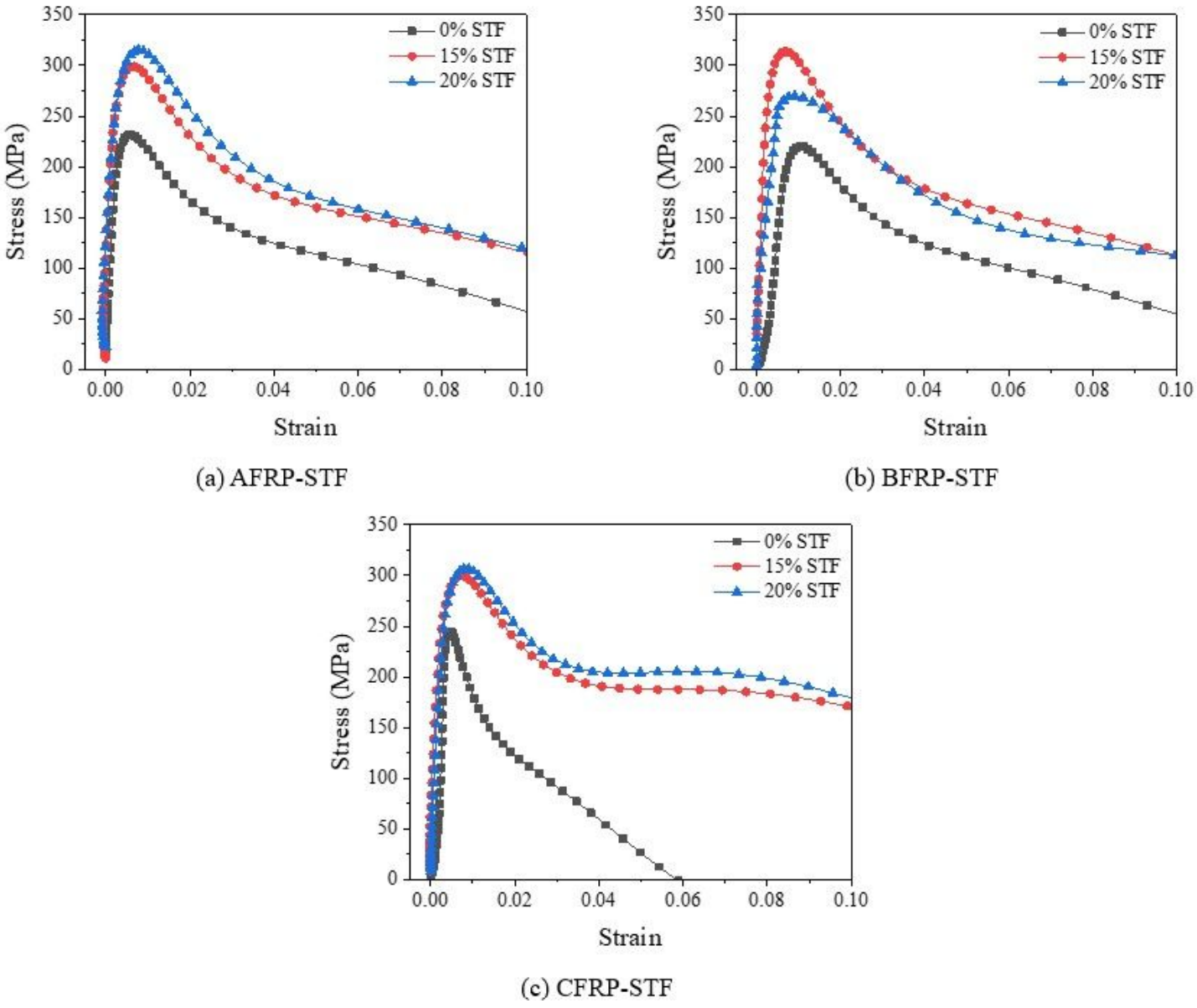

Figure 7

Stress response of AFRP-STF, BFRP-STF, and CFRP-STF at a strain rate of 6100 s^{-1}.

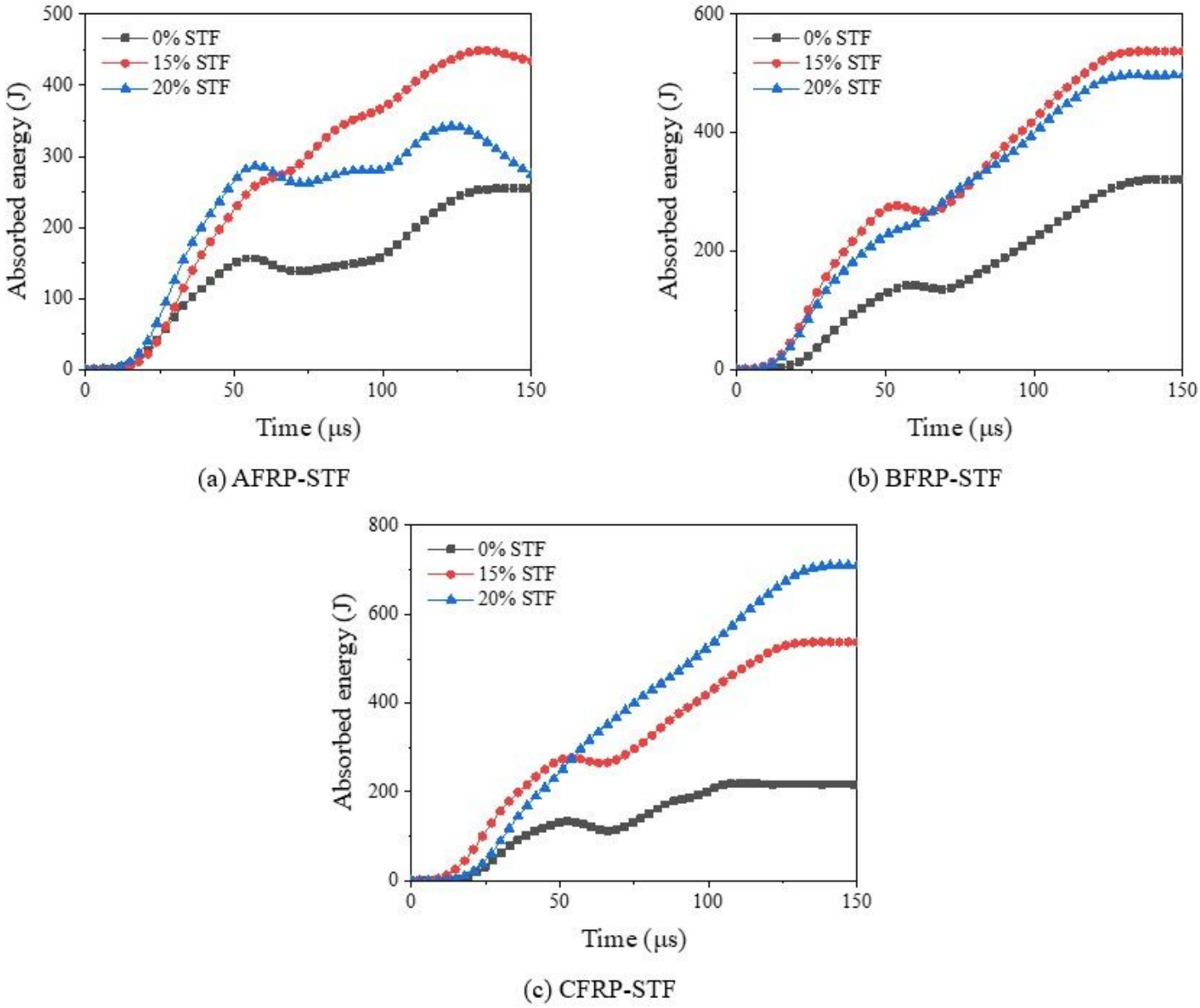

Figure 8

Energy absorption performance of AFRP-STF, BFRP-STF, and CFRP-STF at a strain rate of 6100 s^{-1}.

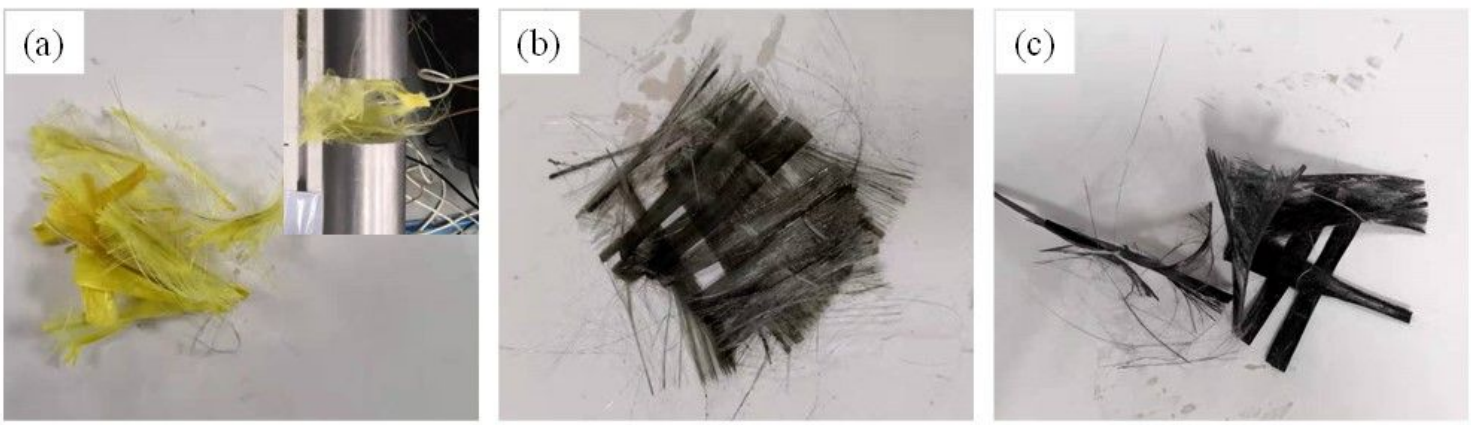

Figure 9

Fields photos of tested specimens after impact at 6100 s^{-1}: (a) AFRP-20%STF; (b) BFRP-20%STF; (c) CFRP-20%STF.

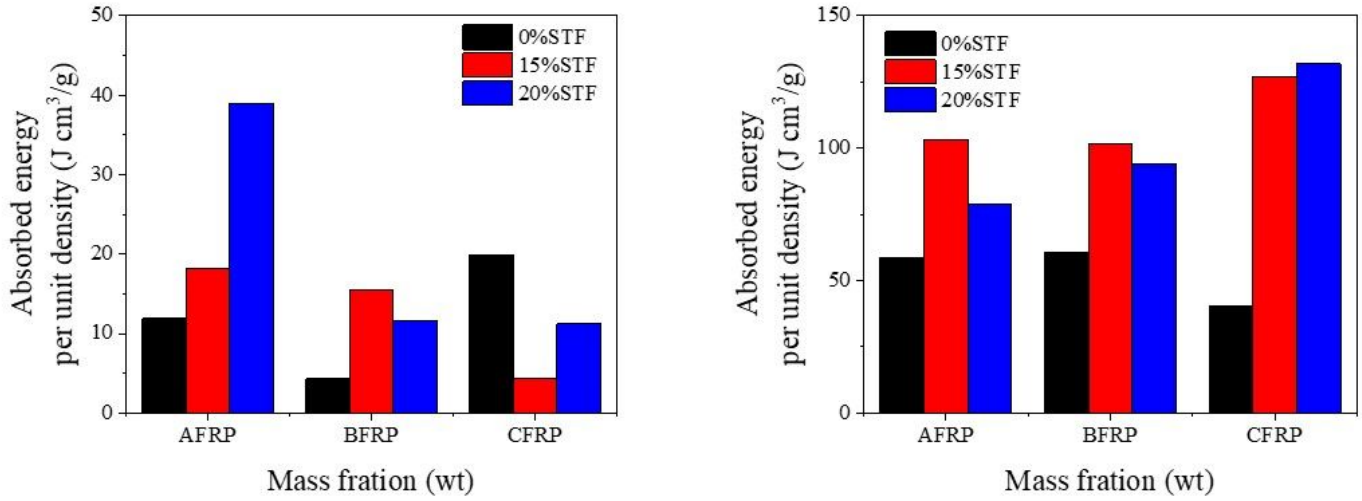

Figure 10

Absorbed energy per unit density of single-layer AFRP-STF, BFRP-STF, and CFRP-STF.

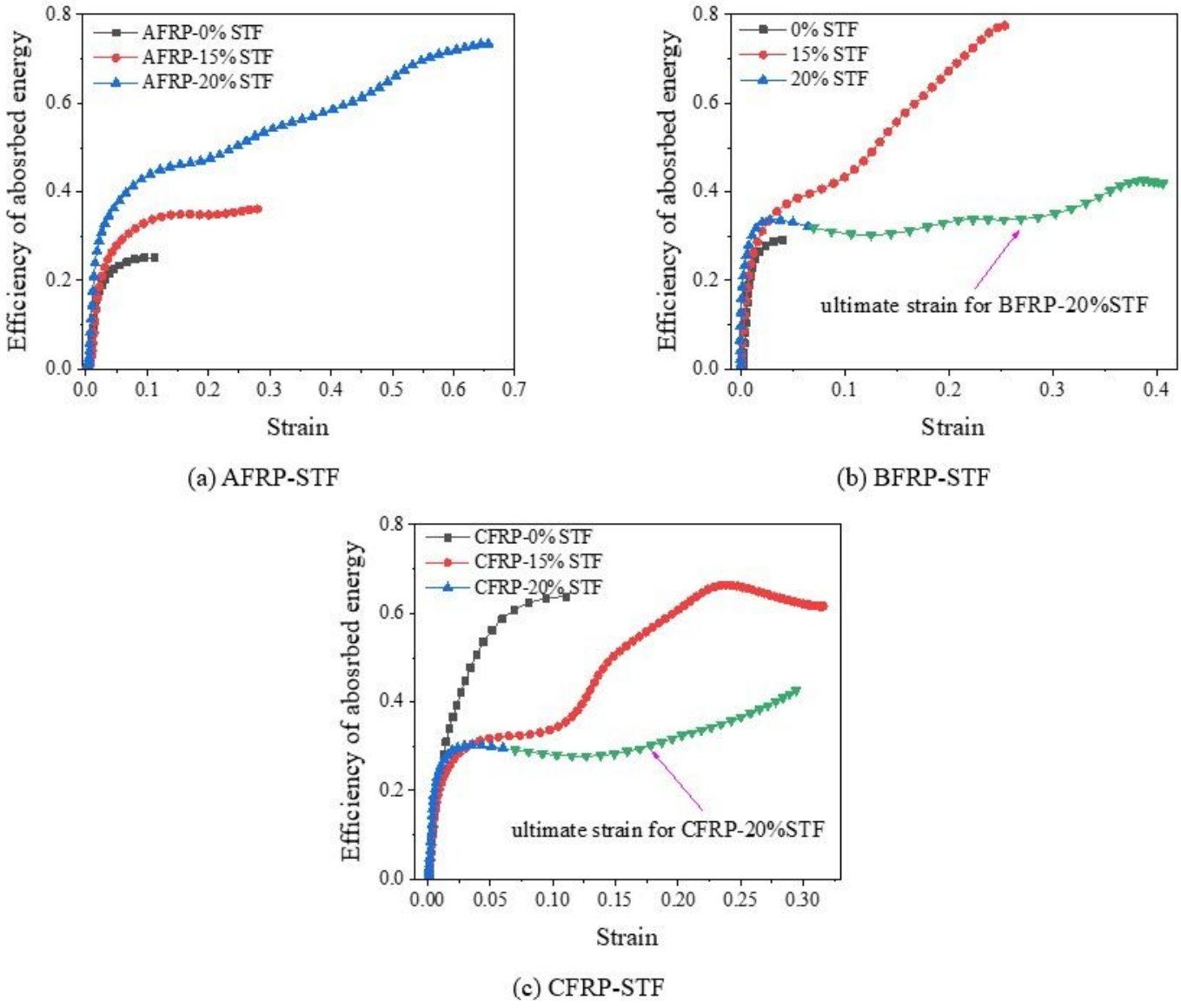

Figure 11

Energy absorbtion rate of AFRP-STF, BFRP-STF and CFRP-STF at strain-rate of 3800 s^{-1}.

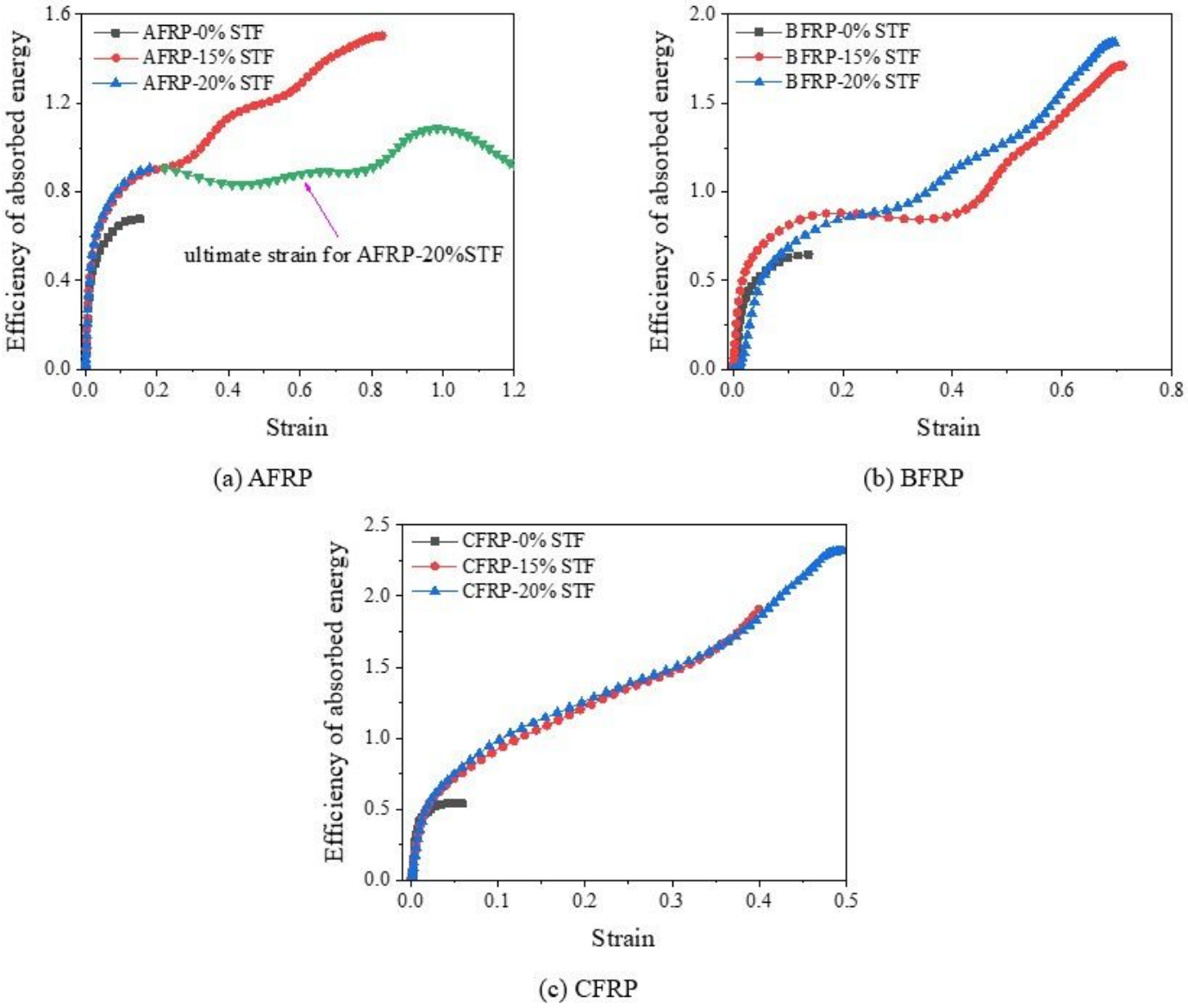

Figure 12

Energy absorbtion rate of AFRP-STF, BFRP-STF and CFRP-STF at strain-rate of 6100 s^{-1}.

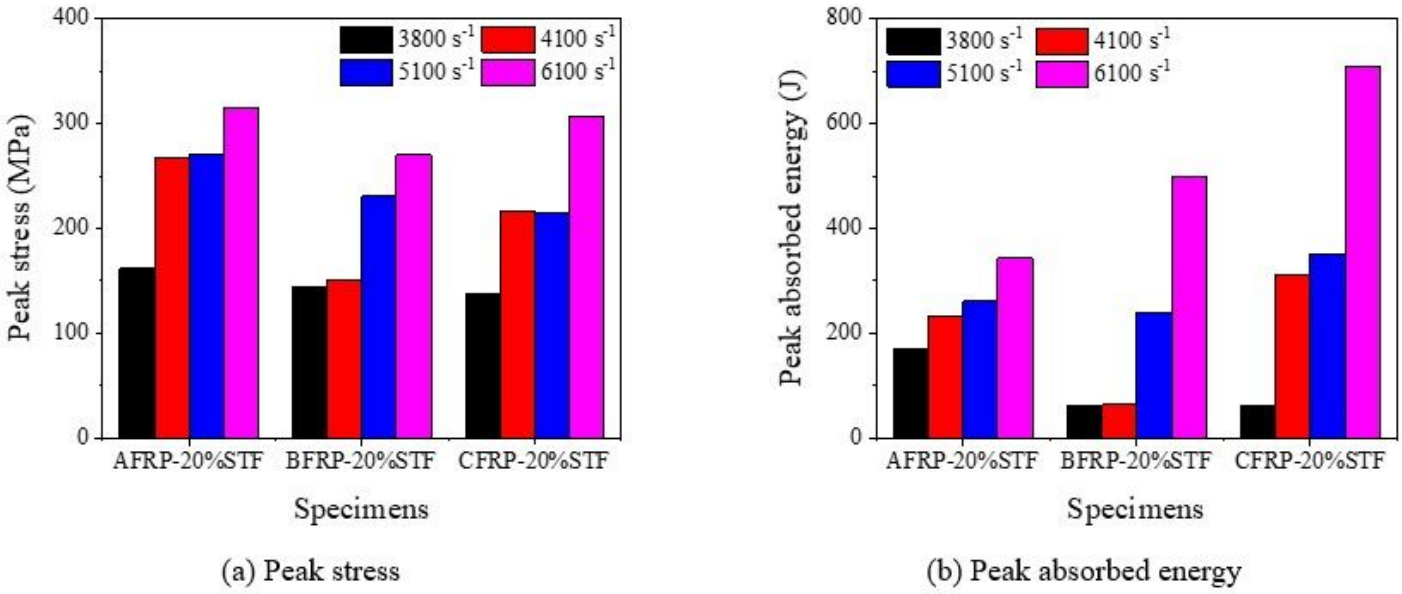

Figure 13

Peak stress and absorbed energy of AFRP-20%STF, BFRP-20%STF, and CFRP-20%STF under different strain rates.